Safe Patient-Led Shoulder Rehabilitation with Biomechanical Model Integrated Collaborative Robot System

MSc Thesis Report

S. Balvert

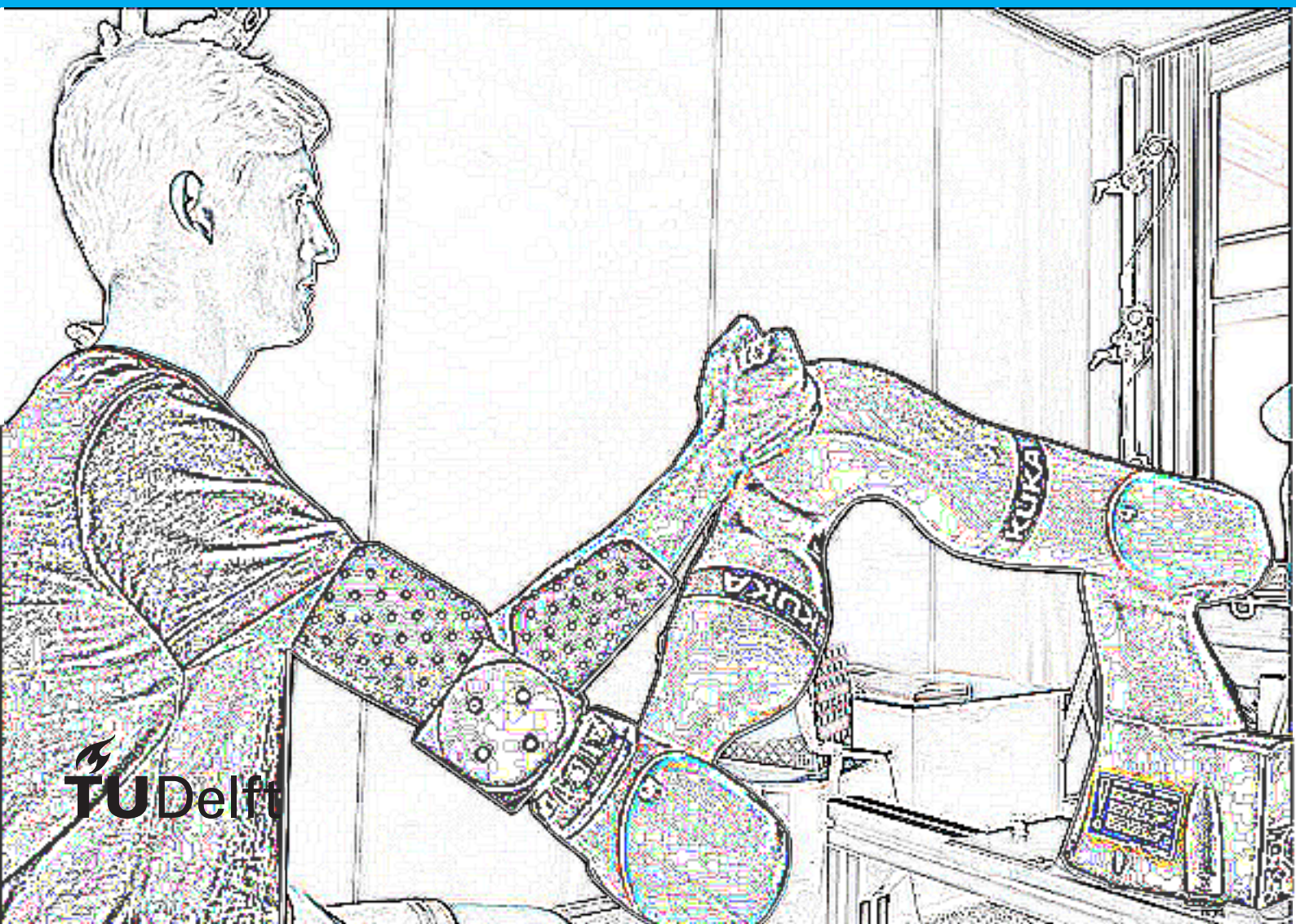

Safe Patient-Led Shoulder Rehabilitation with Biomechanical Model Integrated Collaborative Robot System

by

S. Balvert

to obtain the degree of

Master of Science
in Mechanical Engineering

At the:
Department of Cognitive Robotics,
Delft University of Technology
to be defended publicly on Friday July 15, 2022 at 10:00 AM.

Student number:	4294009	
Supervisors:	Dr. L. Peternel,	TU Delft,
	Dr. A. Seth,	TU Delft,
	Dr. J.M. Prendergast,	TU Delft

TU Delft Delft University of Technology

Preface

It took a while but I finally managed to do it!
First and foremost my sincere thanks and gratitude to my supervisors Luka Peternel and Micah Prendergast, who were indefinitely patient and understanding, and challenged and supported me throughout the lengthy process. I'm especially thankful for all the games of tennis that Dr. Pretendergast let me win. Also thanks to David Abbink, in the few meetings we had he managed to ask sharp and critical questions which improved my final product.

I could not forget the help and input from the rest of the PTbot team: Dr. Ajay Seth, Dr. (to-be) Italo, Tom, Irene, and Noah. It was a joy to be a part of the team, and I appreciate all the suggestions and input. A special thanks to Irene who was always present and ready to mess around with the robot, even though she had better things to do.

Shout out to H421 and the MOKS, if I hadn't been able to let out my energy playing bball I would have imploded long ago.

Of course I could not have done any of this without the support of Rosalie, my parents and my lil' sis.

S. Balvert
Delft, July 2022

Contents

1

Paper

Safe Patient-Led Shoulder Rehabilitation with Biomechanical Model Integrated Collaborative Robot System

Stephan Balvert[1]

Supervised by: J. Micah Prendergast[1], Ajay Seth[2], and Luka Peternel[1]

***Abstract*—In this work, we propose a method for monitoring and management of rotator-cuff tendon strains in human-robot collaborative physical therapy for rotator cuff rehabilitation. The proposed approach integrates a complex offline biomechanical model with a collaborative, industrial robot arm and an impedance controller. The model is used for computing rotator-cuff tendon strain as a function of human shoulder configuration, muscle activation and external forces. This subject- and injury-specific data is stored in *strain maps*, which represent the relationship between the strains and shoulder DoFs. In our previous work, we implemented strain maps to preplan minimal strain, safe trajectories using two shoulder DoFs , and used the corresponding robot-mediated movement for passive trajectory following for healthy subjects. This work expands on that by implementing two novel functionalities: 1) patient-led movement, and 2) adding the third shoulder DoF and the corresponding control complexities, while still controlling for safe rotator-cuff tendon strains. For patient-led movement, we precomputed unsafe zones for each strain map by clustering and fitting ellipses to the clusters. These unsafe areas with increased risk of (re-)injury are then used to set the impedance control parameters and reference pose for real-time biomechanical safety control. By linearly interpolating between strain maps, smooth and safe movement of the third shoulder DoF is added. The resulting robot control torques guide the patient away from unsafe, high strain shoulder poses in real-time during patient-led movement. The proposed method has the potential to improve the safety, Range of Motion, and muscle activity that the patients receive through robot-mediated physical therapy. The main advantage of this approach is that the patient is free to use and explore their full shoulder RoM, while the robot controls and manages biomechanical safety in real-time. To validate the proposed method, we performed two experiments showcasing two novel functionalities, and a third experiment as proof-of-concept displaying the full method.**

***Index Terms*—Biomechanical Model, Rotator-Cuff Rehabilitation, Collaborative Robot, Impedance Control**

I. Introduction

HUMAN safety is the most important aspect of physical Human-Robot Interaction (pHRI), even more so in robot-assisted rehabilitation. To this end, the robot must be aware of the internal state of the patient and their injury risks. In this work, we focus on physical therapy intensive recovery from rotator-cuff injuries of the shoulder as a clinically motivated driving problem. Shoulder rotator-cuff tears alone have an estimated rate of 22.1% in the general population and over 50% for those older than 60 [1]. After injury, with or without surgery, physical therapy to restore shoulder mobility and functionality is a lengthy process.

Author and supervisors are with Cognitive Robotics[1] and BioMechanical Engineering[2] departments of 3Me faculty, Delft University of Technology, Mekelweg 2, 2628 CD Delft, The Netherlands

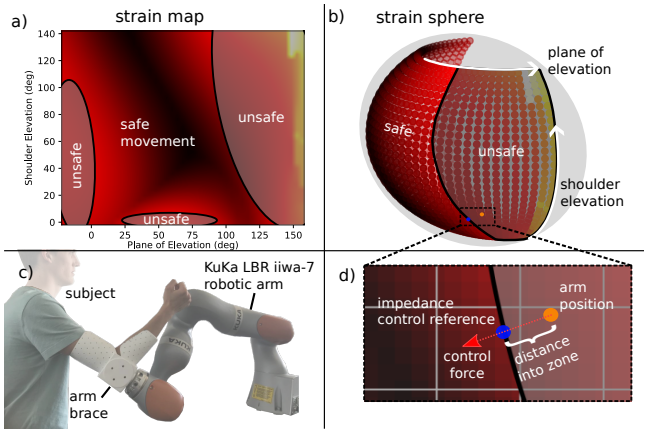

Fig. 1. Physical and biomechanical system setup. a) Strain map which represents the rotator-cuff tendon strains as a function of shoulder DoFs. b) 3D representation of the strain map in Cartesian space, used for robot control. c) A KuKa LBR iiwa-7 robotic manipulator delivers guiding force to the shoulder of a test subject through an arm brace. d) Impedance control force resulting from real-time biomechanical safety control, guiding the subject out of unsafe zones.

Due to the complexity of the shoulder and the risk of reinjury, physical therapy of the shoulder remains conservative even when performed by expert physiotherapists [2]. The conservative nature of physiotherapists means that the amount of therapy delivered is limited and there are many more patients than available physiotherapists at any given time. Furthermore, the work can be quite laborious for the physiotherapists. A promising alternative to classic physiotherapist-based rehabilitation is robotic rehabilitation [3], [4].

Several upper-limb devices have already been developed [3], [4], but they are highly specialized and bulky mechanical systems, expensive and difficult to move between patients. This limits their applicability for clinical therapy. Additionally, to the best of the author's knowledge, these devices do not target rotator-cuff injuries and the corresponding requirements for physical therapy. While custom built robots/exoskeletons can have advantages over industrial collaborative robots in terms of RoM, higher payload, more DoF [5], [6], and possibly

optimized mechanical design for specific task- and kinematic constrains [7]. Mass-produced industrial collaborative robots still have significant advantages for use in assisted physical therapy. They are typically less costly and more readily available than task-specific robots, already meet strict safety criteria for human-robot interaction, and require little additional training to operate.

When applying pHRI for human movement rehabilitation, impedance control offers significant benefits, enabling the modulation of interaction dynamics in real-time through a spring-mass-damper model [8]. The stiffness and damping of the robot can be increased or decreased in varying directions, based on the desired rehabilitation strategy or training intensity [9]–[11]. This method also enables the robot to be soft in certain directions, while being stiff in other directions, allowing the robot to act as a guide for the human. Additionally, the formulation enables easy incorporation of gravity compensation terms for the human arm. Nevertheless, impedance control on its own, usually cannot guarantee the safety of the human with which the robot is interacting.

Previous research on safety of pHRI has predominantly focused on external safety, in terms of: collision detection and avoidance [12], [13], soft robots [14], [15], compliant actuators [16], influence of robot joint configuration on collision injury [17], awareness of potential injury caused by human-robot collisions [18], [19], and conservative force/velocity limits [20]. However, often the proposed model- and metric-based rating of a robot's external safety characteristics are insufficiently consistent with medically observed injury [21].

Recently, heuristic ergonomics has been used to calculate internal safety in pHRI in real-time [22], [23]. Methods such as, Rapid Upper Limb Assessment (RULA) [24] and Rapid Entire Body Assessment (REBA) [25], are used to evaluate the ergonomics of working postures of the upper limbs and the entire body respectively, resulting in a score that quantifies the safety of the worker's posture. This score can be used to provide a quick assessment of the muscle function and the experienced external load that the person is undergoing, giving an indication of the level of risk for induced musculoskeletal disorder (MSD) risk. However, it is hard to adjust the results for human-specific parameters and difficult to generalize them for specific tasks or conditions.

This is solved by using biomechanical and musculoskeletal models, which can account for patient-specific parameters and give an accurate estimation of the actual internal properties of the human body; such as, (static) joint loading [26], muscle fatigue [27], muscle comfort [28], and muscle manipulability [29]. These methods are very promising, but have mainly been applied to industrial scenarios, not clinical scenarios.

A few recent studies focused on shoulder rehabilitation using industrial collaborative robot arms. In [30], the authors proposed a method where the control of the collaborative robot arm was based on the measurements of human arm pose and muscle activity through electromyography and used to perform shoulder rehabilitation. The method in [31] proposed to gather physical (force, position, etc.) and psychophysiological (EMG, EEG, etc.) measurement data from various sensory systems and used a collaborative robot arm for upper arm rehabilitation. However, these methods did not integrate biomechanical models of the human shoulder/arm, thus had limited knowledge of the internal state of the human. Without accurate perception of the complex internal dynamics, injury risks during robotic physical therapy can not be properly mitigated. Additionally, these methods also did not target physical therapy and rotator cuff injury.

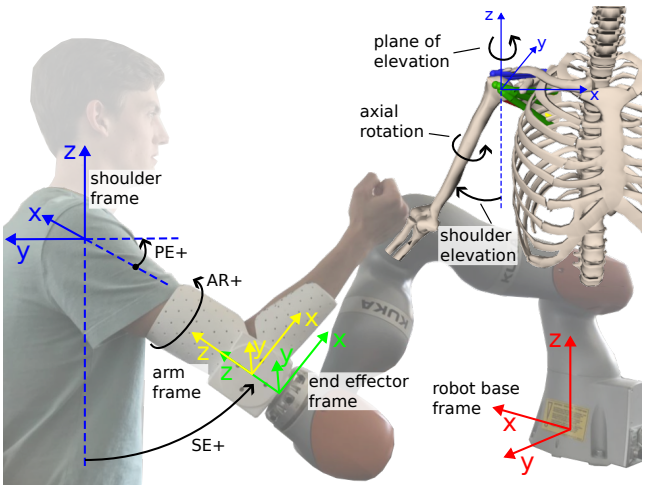

Fig. 2. The shoulder DoFs are shown here: Plane of Elevation is a rotation around the shoulder z-axis, Shoulder Elevation is the angle between the negative shoulder z-axis and the arm, and Axial Rotation is around the z-axis of the arm frame. The shoulder frame, arm frame, end effector frame, and robot base frame are used to compute the shoulder DoFs from the robot end effector pose and vice versa.

Our previous work in [32] integrated an industrial collaborative robot and a complex biomechanical model of the human shoulder for delivery of safe physical therapy in rotator-cuff rehabilitation. We introduced the concept of strain maps; a 2D representation of strain on each of the four rotator-cuff muscle tendons. The strain maps are calculated for human arm poses described by three Degrees of Freedom (DoF) of the shoulder. The method used impedance control for upper arm trajectory tracking through the strain map, keeping the rotator-cuff muscle strains below a safety threshold and minimizing cumulative strain along the preplanned trajectory, mainly suitable for early stages of rehabilitation. This method allowed two degrees of freedom for the subject, while the third was fixed. This limits the RoM significantly, which, along with therapy time, typically needs to be maximized for effective physical therapy [33].

To address this problem, we propose human arm movement using all three shoulder DoF, and allowing the patient to move around freely without constraining them to a trajectory: patient-led movement. This increases the RoM available to the patient and results in a system more suitable for stages of rehabilitation where the patient dictates the movement. The patient-specific biomechanical model is incorporated with an industrial collaborative robot using impedance control for human safety in terms of rotator-cuff muscle strains in real-time. To this end, we use the strain maps and the biomechanical model described in [32]. The proposed method is demonstrated and evaluated with proof of concept experiments on a KuKa

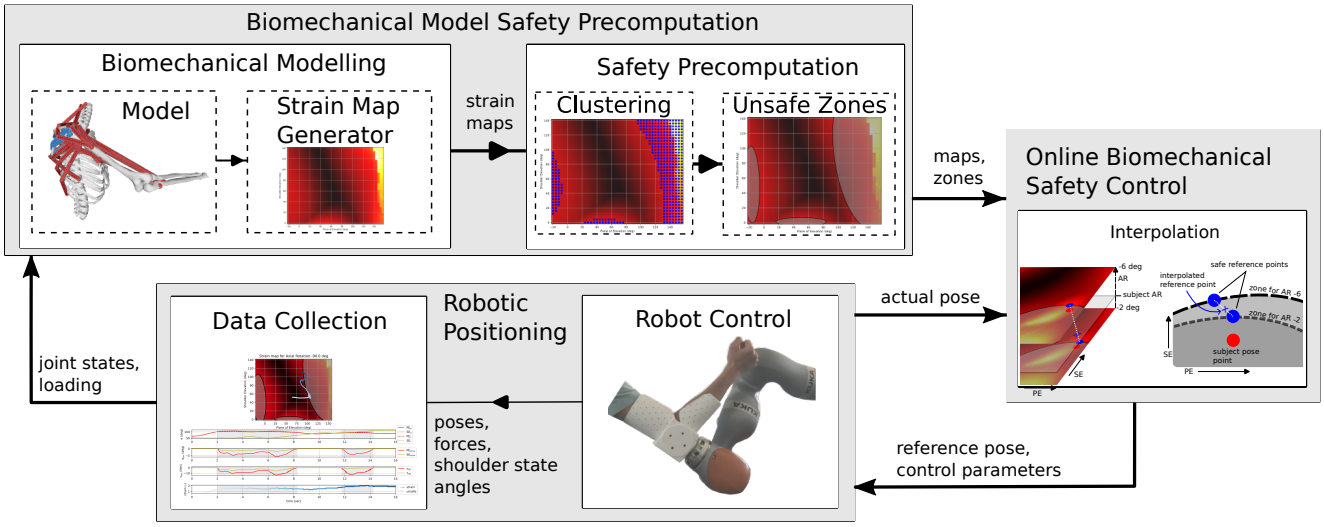

Fig. 3. Workflow of the biomechanics aware robot system for robot-assisted shoulder rehabilitation. The biomechanical model is used to generate maps of the rotator-cuff muscle strains. Unsafe zones, where the strain is above a set threshold for increased risks of (re-)injury, are calculated through clustering and fitting minimal volume enclosing ellipses to the clusters. The unsafe zones are used to compute the impedance control reference in real time by linear interpolation of the two closest strain maps, using the actual robot end effector pose. The resulting Cartesian forces are converted to Robot torques through which the collaborative robot guides the human out of unsafe zones. Data is collected from the robot for further evaluation.

LBR iiwa-7 collaborative robot arm.

II. Methodology

This section presents the methodology that has been used in the current work. II-A Explains how we compute strain maps using biomechanical modelling, and how these maps are used to precompute unsafe zones in the shoulder state space. II-B Shows how these unsafe zones are used to calculate safe reference points in real-time and dictates the transformation between robot Cartesian frame and shoulder state angles. II-C Presents the use of impedance control to manage rotator cuff strains of the human during patient-led shoulder rehabilitation movements. Fig 3 presents the workflow that was followed.

A. Strain map computation and safety

We used the open-source computational musculoskeletal modeling tool OpenSim [34] to create strain maps. This software can be used to create biometrically scaled subject models and analyze those at a high degree of fidelity with a large range of physical input dynamics (both internal, e.g., muscle activations, and external, e.g. applied forces). OpenSim and the Thoracoscapular Shoulder Model [35] were used to compute the strain of all four rotator-cuff muscles for any pose of the subject's arm within their range of motion. This strain data as a function of three shoulder DoF is represented by *strain maps*, Fig. 1 a). This requires the external loads and their location, and position and velocity of the human shoulder model (joints). The strain maps are used to inform the robot about the (re-)injury risks of the subject rotator-cuff muscles in real-time. If the strain in one or more rotator-cuff muscles is above a certain (strain) threshold, the muscle/tendon may be reinjured, likely resulting in patient discomfort, pain, and lengthier rehabilitation. Currently, physio therapists are constrained to instruct conservative movements as they only have qualitative measures to sense muscle strain. The strain maps can be integrated with the robotic system to gain a quantitative sense of subject safety in terms of muscle strain, allowing for less conservative, safe exercises with an expanded range of motion.

We consider the three degrees of freedom that constitute motion of the upper arm (humerus) relative to the shoulder blade (scapula) as the rotator-cuff muscles span the gleno-humeral joint, Fig. 2. These are: Axial Rotation (AR, internal and external rotation) with a range of motion of -90 to 90 degrees, Plane of Elevation (PE, the plane in which the arm is moved) with a feasible range of -20 to 160 degrees, and Shoulder Elevation (SE, horizontal abduction) with a feasible range of 0 to 144 degrees. These three DoF comprise the shoulder state vector as

$$\boldsymbol{\alpha} = [\text{AR, PE, SE}],$$

where all angles are in degrees. The strain map is determined by AR, and PE and SE are, respectively, the x- and y-coordinates on the strain map, Fig. 5).

All strain maps were precomputed for the entire range of motion for each muscle at varying velocities and muscle activations, this allows for real-time implementation of the strain data from the complex biomechanical model. The speed of the arm and the level of activation of all four rotator-cuff muscles were set, and the humerus was posed in all combinations of the three DoF of the glenohumeral joint, using 4 degree increments. All strain maps were computed offline for the subject and stored in the system to be used by the robot. Readers interested in further information on the computation of the strain maps are referred to Section II.A in our previous work [32].

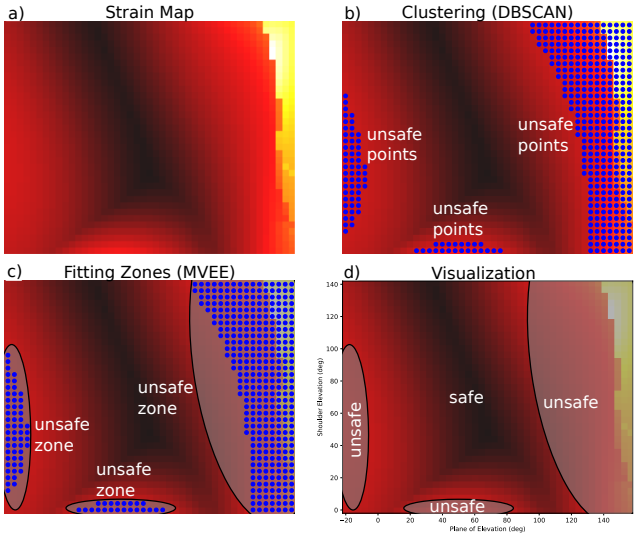

Fig. 4. Workflow of precomputing unsafe zones on strain maps for real-time biomechanical safety visualization and control. a) shows the strain map as output by the biomechanical model. b) shows the clustering, using DBSCAN, of the unsafe points where the rotator-cuff strain is above a specific threshold for increased risk of re-tearing the tendons. In c) the Minimum Volume Enclosing Ellipses (MVEE) are calculated for all clusters, they represent the unsafe zones on the strain map and are used in the controller. d) shows the resulting visualization the patients and PTs are shown, indicating the safe and unsafe zones on the strain map.

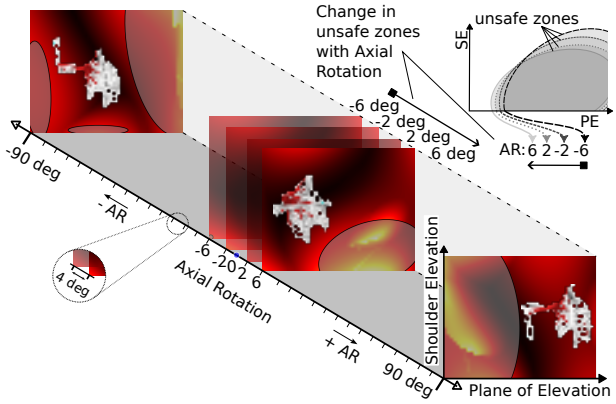

Fig. 5. Change of strain maps and unsafe zones with Axial Rotation. The strain maps are spaced 4deg apart from -90 to 90 degrees Axial Rotation. The arm poses are overlaid on the corresponding strain maps. The top right shows the change in the unsafe zones for four overlaid strain maps (6, 2, -2, -6 deg AR).

For the strain maps to be integrated with the robot system, we defined unsafe zones for each strain map for clusters where the strain was above the set strain threshold. This threshold is subject and injury specific, and changes with rehabilitation progress, strain values above this threshold indicate the patient is at risk of (re-)injury.

The unsafe points on a map were then clustered, Fig. 4 b), using Density-Based Spatial Clustering of Applications with Noise (DBSCAN) [36]. This method is computationally inexpensive, suited for identifying clusters of non-spherical shapes, and works well for data sets with a constant density and low-dimensional spaces. Another advantage of using DBSCAN is that, after setting the parameters, it needs no further supervision, as there are hundreds of strain maps per subject, this is an important feature. Inputs to this method are the minimum cluster size and ϵ. The minimum cluster size was set to one, as even a single unsafe strain point should be avoided by the subject, thus identified as a cluster. ϵ is the maximum distance between two samples for one to be considered as in the neighborhood of the other. It was calculated as function of the strain map step size in degrees, such that clusters can span diagonal gaps.

After clustering all unsafe points on a strain map, the Minimum Volume Enclosing Ellipse (MVEE) of each cluster defines the unsafe zone, Fig. 4 c). Using ellipses to define the zones benefited computational costs, as the ellipse parameters can be used to check whether a point is in an ellipse, thus unsafe, and if so to calculate the closest point on the ellipse contour, i.e. the closest point with safe strain. Brent's method [37] was used to estimate the closest point on the ellipse boundary, as further detailed in Appendix A.2. This ensures smooth and continuous calculation of reference points once a subject entered an unsafe zone, however it leads to a more conservative zone boundary as safe points can be included. This approach was chosen over defining the unsafe zones using concave hulls of the clusters, as this led to switching behaviour when the reference point 'jumped' when equidistant lines were crossed, leading to impedance control force spikes. However, this approach only includes unsafe points in the zones, thus is less conservative than the MVEE method.

B. Strain map based control

To integrate the strain map based safety into the robot impedance controller in real time, every time step we need to

1) calculate the actual shoulder state vector;
2) perform a biomechanical safety check for the subject;
3) update the impedance control parameters and the reference pose accordingly

To prevent the subject from entering the unsafe zones, we first need to calculate the actual subject shoulder state vector, $\boldsymbol{\alpha}_a$, which defines the current strain map and the subject's position on that map. This can be computed from the human arm pose, $\boldsymbol{x}_{arm}$, expressed in the human shoulder frame. The lower arm of the subject is strapped into the arm brace, which is attached to the Robot End Effector; We compute $\boldsymbol{x}_{arm}$ in the Robot Frame using the Robot End Effector pose $\boldsymbol{x}_{ee}$, and the angular and positional offset of the brace to the End Effector. The origin of the arm frame is at the elbow, the x-axis points towards the wrist, and the z-axis towards the shoulder, Fig. 2, the lower arm is constrained by the brace at a 90 degree angle to the upper arm. The shoulder pose is assumed to remain constant over time, as subjects are instructed not to move it. Once we know the pose of the arm in the frame of the shoulder, we can calculate the actual shoulder state vector $\boldsymbol{\alpha}_a$. The transformation from the robot end effector pose to $\boldsymbol{\alpha}_a$ is described in Appendix B.2.

We then perform a biomechanical safety check for the subject, using $\boldsymbol{\alpha}_a$ and the strain maps. However, as the unsafe

zones are calculated for each strain map, and the maps change with AR, so do the unsafe zones, Fig. 5. This Figure shows the change of the strain maps with AR, and in the top-right the change of the unsafe zones for adjacent strain maps. As the maps are discretely spaced 4 deg apart in AR direction, and patient movement is continuous, the patient will (almost) never be on exactly one strain map. Instead, the subject will always be between two strain maps where one of the two is closest. The closest map is the current strain map, and is shown to the patient and the physiotherapist, Fig. 4 d). As the unsafe zones differ per strain map, this means that the subject can be safe on one map but would be unsafe in the other adjacent map. This needs to be accounted for in the controller.

We calculate the closest safe point on both adjacent strain maps, to $\boldsymbol{\alpha}_a$, and linearly interpolate between those using the actual subject Axial Rotation, Fig. 6. If the point on an adjacent map is in an unsafe zone, the ellipse equations are used to estimate the closest point on the ellipse contour, this is the closest safe point on that strain map. Otherwise, the point on the adjacent map is safe and is used for the linear interpolation. Appendix A details the ellipse equation used and the algorithm for estimating the closest point on the ellipse contour.

The linearly interpolated reference shoulder state angles vector, $\boldsymbol{\alpha}_r$, is then used to calculate the reference pose for the human arm and in turn the robot end effector. Appendix B.1 details the calculation of the robot end effector pose from the shoulder state angles. The impedance control parameters and the reference pose are set according to the biomechanical safety check. This way, the robot system implements quantitative knowledge of the subject internal safety expressed in rotator-cuff muscle strain.

C. Robot Control

To implement the biomechanical safety the robot was controlled by a Cartesian impedance controller [8], defined as

$$\boldsymbol{F}_{imp} = \boldsymbol{K}\big(\boldsymbol{x}_r - \boldsymbol{x}_a\big) + \boldsymbol{D}\big(\dot{\boldsymbol{x}}_r - \dot{\boldsymbol{x}}_a\big), \tag{1}$$

where $\boldsymbol{F}_{imp} \in \mathbb{R}^6$ is the interaction force vector acting from the robot on the patient, $\boldsymbol{K}$, $\boldsymbol{D} \in \mathbb{R}^{6\times6}$ are the desired stiffness and damping matrices in Cartesian space, respectively, while $\boldsymbol{x}_a$, $\dot{\boldsymbol{x}}_a \in \mathbb{R}^6$ are the actual end effector pose and velocity, and $\boldsymbol{x}_r$, $\dot{\boldsymbol{x}}_r \in \mathbb{R}^6$ are the reference pose and velocity vectors.

To adjust the stiffness in particular directions, the stiffness matrix can be non-diagonal, with the principal axes rotated in the robot base frame. The damping matrix is rotated equally and was obtained using double diagonalisation design [38], dependant on the stiffness matrix as

$$\boldsymbol{D} = 2\boldsymbol{Q}\boldsymbol{D}_\xi\sqrt{\boldsymbol{K}_0}\boldsymbol{Q}^T, \tag{2}$$

where $\boldsymbol{Q}$, $\boldsymbol{K}_0 \in \mathbb{R}^{6\times6}$ are, respectively, the eigenvectors and eigenvalues obtained by the eigendecomposition of the stiffness matrix $\boldsymbol{K} = \boldsymbol{Q}\boldsymbol{K}_0\boldsymbol{Q}^T$. The diagonal matrix $\boldsymbol{D}_\xi \in \mathbb{R}^{6\times6}$ contains damping factors, which were set to 0.7.

We controlled the desired Cartesian force, expressed in the robot base frame, through the robot joint torques as

$$\boldsymbol{\tau} = \boldsymbol{M}(\boldsymbol{q})\ddot{\boldsymbol{q}} + \boldsymbol{C}(\boldsymbol{q},\dot{\boldsymbol{q}})\dot{\boldsymbol{q}} + \boldsymbol{g}(\boldsymbol{q}) + \boldsymbol{J}(\boldsymbol{q})^T\big(\boldsymbol{F}_{imp} + \boldsymbol{F}_g(\boldsymbol{q}_h)\big), \tag{3}$$

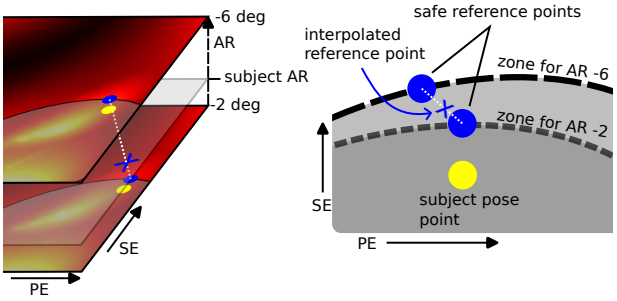

Fig. 6. Linear interpolation between the two reference points of the two adjacent strain maps to the subject shoulder state angles. Shown here, for subject pose AR -3deg and the two adjacent strain maps for AR -2 and -6 degrees. PE and SE for the subject are the same on both adjacent maps.

where $\boldsymbol{\tau}$, $\boldsymbol{q} \in \mathbb{R}^7$ are vectors of robot joint torques and robot joint angles respectively, $\boldsymbol{g} \in \mathbb{R}^7$ is the gravity vector, and $\boldsymbol{J} \in \mathbb{R}^{6\times7}$, $\boldsymbol{M}$ and $\boldsymbol{C} \in \mathbb{R}^{7\times7}$ are the robot Jacobian matrix, mass matrix, and Coriolis and centrifugal matrix, respectively. $\boldsymbol{F}_g \in \mathbb{R}^6$ is a vector for gravity compensation of the human arm, dependent on the human shoulder configuration $\boldsymbol{q}_h$, and $\boldsymbol{F}_{imp} \in \mathbb{R}^6$ is the desired impedance control force which follows from (1).

The reference pose $\boldsymbol{x}_r$ for the impedance controller was calculated from the linearly interpolated reference point from the strain maps. If the current shoulder state angles are in an unsafe zone in either, or both of the two closest strain maps, the impedance control stiffness matrix is set to high stiffness $\boldsymbol{K}_{hi}$, the damping matrix is changed accordingly using (2). If the current pose is safe on both closest maps, the impedance control stiffness matrix is set to low stiffness $\boldsymbol{K}_{lo}$, the damping matrix is set accordingly. Where $\boldsymbol{K}_{hi} = \text{diag}[k_{hi\_p}, k_{hi\_p}, k_{hi\_p}, k_{hi\_r}, k_{hi\_r}, k_{hi\_r}]$ and $\boldsymbol{K}_{lo} = \text{diag}[k_{lo\_p}, k_{lo\_p}, k_{lo\_p}, k_{lo\_r}, k_{lo\_r}, k_{lo\_r}]$, with k_{hi_p} and k_{lo_p}, respectively, the high and low positional stiffness (N/m), and k_{hi_r} and k_{lo_r}, respectively, the high and low rotational stiffness (Nm/rad).

This results in a control force guiding the subject out of the unsafe zones, perpendicular to the zone boundary, to the closest point on the zone boundary. If the current point is not in an unsafe zone, the reference point is set to the current coordinates, thus the impedance control is not active. For data analysis the Cartesian impedance control force on the end effector is transformed to torques on the human shoulder joint expressed in the three shoulder DoF directions, this conversion is detailed in Appendix B.3.

III. Experiments

The first part of this section covers the general experimental setup, and control parameters. The experimental evaluation of the proposed method was done through three experiments: the first two experiments showcase the two functionalities that make up our method, and the third shows the complete method where both functionalities are implemented simultaneously.

In the first experiment, the subjects were allowed to move freely on one strain map, but not move to other strain maps.

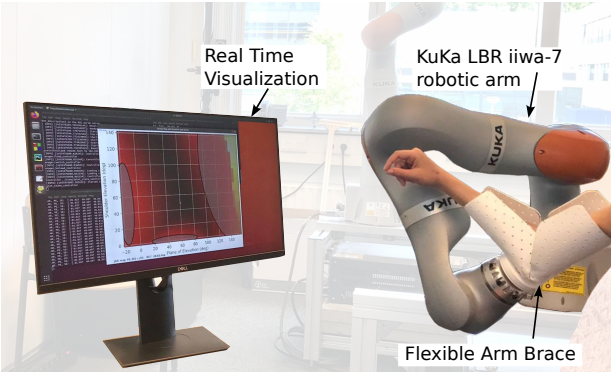

Fig. 7. The experimental setup used in this work. The KuKa iiwa-7 industrial robot arm delivers forces to the subject arm through the flexible brace whenever the subject entered an unsafe zone. This was simultaneously shown on the visualization interface, through which the subjects got real-time feedback on the shoulder state angles, updating the strain map with unsafe zones, and their positions accordingly.

This is similar to our previous work, in that Axial Rotation is fixed during the experiment, i.e., the subject stays on one strain map. Unlike our previous work, which was limited to the robot enforcing a pre-planned trajectory, the subject is free to move on the strain map and interact with unsafe zones.

In the second experiment, the subjects were free to move between strain maps, but not move around on the strain maps. To this end, the subject's position, PE and SE, on the strain maps was constrained, while allowing free movement, AR, between the strain maps. This showcases the real-time safety control while switching between the unsafe zones in different maps.

The third experiment is the proof-of-concept of the research described in this work, combining the first two experiments. This allowed the subjects to move around on and between strain maps, resulting in unconstrained movement of all three shoulder state angles, while using impedance control for strain map based safety, activated when subjects entered the previously defined unsafe zones.

The study was approved by the Human Research Ethics Committee of Delft University of Technology.

A. Experimental Setup

The arm brace designed in our previous work was used for these experiments. The brace was mounted to the robot such that when the subject entered the brace, the upper arm was in line with the robot end effector Z-axis, which allowed control of Axial Rotation through the orientation reference of the end effector Z-axis, while Plane of Elevation and Shoulder Elevation were controlled using the remaining DoF. The industrial robot used is a KuKa LBR iiwa-7 collaborative robot. Fig. 7 shows the experimental setup.

Subject torso height and arm length were used to update the control method by setting the shoulder origin in the robot frame, and this ensured the correct positioning and sizing of the strain sphere, Fig. 1 b), for each subject. Human shoulder pose in the robot frame was assumed constant over time as the subjects were instructed to try and minimize shoulder translation.

The robot was moved to its initial pose before the subject was seated. Once the subject was seated, the subject entered the brace and was secured with a velcro strap. When the subject indicated to be ready, the experiment was started by the experiment via a keyboard interface. Subjects were provided visual feedback during the experiment of the strain map they were closest to and on that map: color gradient to indicate rotator cuff strains, the unsafe zones, their position, and the reference position (if applicable). The visualisation was updated with 30 frames per second. The control loop was executed at approx. 200 Hz.

The stiffness values used in the experiments for the impedance controller were: positional $k_{hi\_p} = 800$ N/m, $k_{lo\_p} = 400$ N/m, rotational $k_{hi\_r} = 30$ Nm/rad, and $k_{lo\_r} = 15$ Nm/rad. The damping matrices were calculated accordingly, using the double diagonalization design in (2). The strain threshold to precompute the unsafe zones for the strain maps used in the experiments, was set to 2.4 (-).

For each experiment actual- and reference poses of the robot end effector, impedance control force in robot base frame, and actual- and reference shoulder state angles were recorded and stored.

B. Exp 1: Moving on one strain map

We first applied the proposed method to safe movement on one strain map, this allowed the subject to move freely on the map instead of following a trajectory, as was shown in our previous work. For this experiment, Axial Rotation was constrained to -90 degrees. To make the subject stay on this strain map, the reference for AR was kept constant at this angle. The subject was free to move, varying PE and SE. The references for these shoulder state angles were calculated in real-time according our method, depending on the interaction with unsafe zones.

The subject started the experiment at -90 deg. AR, 65 deg. PE and 55 deg. SE. After the subject was strapped into the brace in the initial pose and was ready to begin, the experiment was started. The results for this experiment are shown in Fig. 8. The top plot shows the strain map for the constant Axial Rotation with PE on the x-axis and SE on the y-axis. The colorbar on the right of the map indicates the maximum strain of the four rotator-cuff tendons for each point, as shown on the map. The unsafe zones are highlighted in grey, and the trajectory during the experiment is represented by the white-to-blue color gradient line. The same color gradient line is shown in the top graph, which depicts the strain vs time during the experiment trajectory.

The second graph shows α_a (solid lines) and α_r (dotted lines) in degrees over time, AR is left out as it was kept constant during the experiment. The third graph shows the shoulder state angles errors over time, where again AR has been left out. The error is calculated as $\alpha_r - \alpha_a$, which can be seen to be nonzero only when the subject is in an unsafe zone (highlighted grey areas). This means the impedance controller was only active when the subject entered the unsafe zones on the strain map.

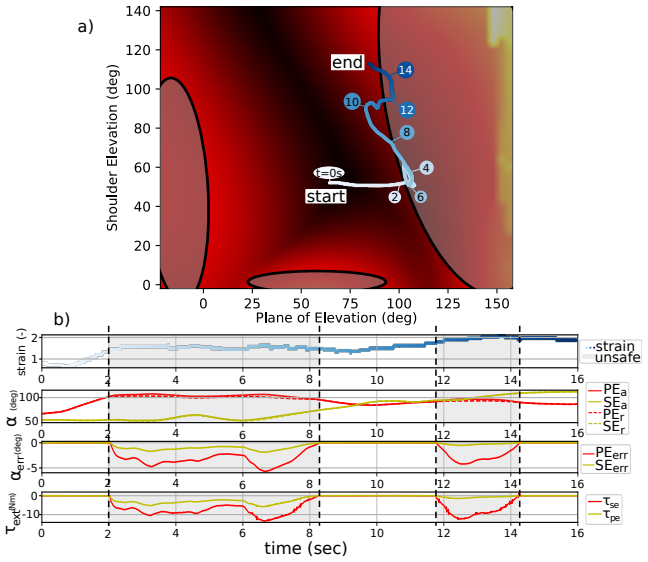

Fig. 8. Results of fixed axial rotation experiment for one subject, where subject movement was constrained to one strain map. The strain map in a) shows the trajectory on the strain map, which was fixed at -90 degrees Axial Rotation, the color gradient of the trajectory matches with the first graph to indicate temporal coherence. The colorbar on the right indicates rotator-cuff tendon strain for each point on the map. In c) the results are shown in graphs, the first graph shows the estimated strain during the experiment, where the color gradient matches the trajectory on the strain map, and the grey areas indicate that the subject was in an unsafe zone at that time. The second graph shows the actual, α_a, and reference, α_r, shoulder state angles for Plane of Elevation and Shoulder Elevation. Axial Rotation is not shown as it was fixed for the duration of the experiment. The third graph shows the errors for the same shoulder state angles. The bottom graph shows the resulting impedance control torques, acting on the subject, expressed in the directions of the shoulder state coordinates PE and SE.

From the reference shoulder state angles, the Cartesian reference pose for the robot end effector expressed in the robot base frame was calculated. Then the impedance controller, in (1), resulted in a force from the robot on the human, exerted at the end effector. This load vector, with forces and moments, was then used to calculate the control torques in the shoulder state space, i.e. torques in the directions of the shoulder state angles: τ_{AR}, τ_{PE}, and τ_{SE}, respectively. These are shown in the bottom graph for PE and SE.

The torques increase rapidly when the subject enters an unsafe zone, which can be seen around 2 and 11.8 seconds. Comparing the shoulder state angles errors from the third graph with the shoulder state control torques shows that the external control force acts in the same direction as the shoulder state errors; the impedance controller forces the subject towards the closest point on the zone boundary, which is the closest safe point in terms of strain. It also shows that when the subject exits an unsafe zone, the shoulder state torques smoothly decrease to zero again. When the subject entered the unsafe zone for the second time, after moving up on the map, the resulting shoulder state torques are mostly in the negative PE-direction. This makes sense, as the zone outline is almost vertical at these points and the control torque always points towards the closest safe point on the zone boundary.

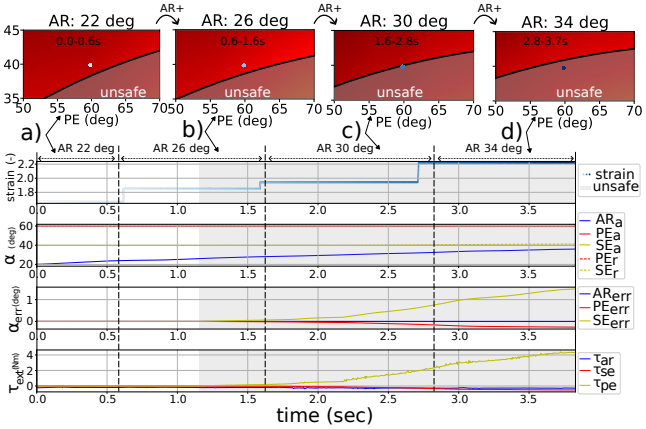

Fig. 9. Results of the experiment showcasing movement between strain maps for one subject, where the subject's position on the maps, in terms of PE and SE, was fixed, and the subject was free to move AR (changing strain maps). The four strain maps on top show the trajectory and the unsafe zones, the color gradient of the trajectory matches with the first graph to indicate temporal coherence. The first graph shows the estimated strain during the experiment, where the color-gradient matches the trajectory on the strain maps, and the grey area indicates that the subject was in an unsafe zone at that time. The second graph shows the actual, α_a, and reference, α_r, shoulder state angles, the reference for AR is not shown as it was equal to the actual value during the experiment. The third graph shows the shoulder state angles errors used for the impedance controller. The bottom graph shows the resulting impedance control torques, acting on the subject, expressed in the directions of the shoulder state coordinates.

C. Exp 2: Moving between strain maps

To grant the patients free movement in all three shoulder state angles, in addition to moving on a strain map as shown in the first experiment, they need to be able to move between strain maps. As this also changes the unsafe zones, the reference shoulder state angles will differ per map for the same PE, SE position on each map. This can mean the subject is safe on the current strain map, but is in an unsafe zone on the adjacent strain map. To prevent impedance control force jumps caused by the change of magnitude and direction of α_r due to new zones, the reference point is calculated by linearly interpolating the reference points of the two closest strain maps at each time step, Fig. 6. The reference point changes gradually, allowing smooth transitions between strain maps

For this experiment, the subject was free to move between strain maps, but constrained to a fixed position on these maps, i.e., the subject was free to change Axial Rotation, while Plane of elevation and shoulder elevation were constrained. The subjects started in a safe part of the strain map at 22 deg AR and [PE,SE] = [60, 40] deg. They were allowed to explore the full AR range to the extent they felt comfortable.

The results of this experiment are shown in Fig. 9. It shows a sample of the experiment, representing three, out of four, important scenarios when dealing with changing strain maps. The four strain maps on top are for AR 22, 26, 30, and 34 degrees, respectively, and show the trajectory of the subject and the unsafe zones. The time intervals where the subject was on each strain map are labeled a) through d), where a) is the time interval spent on the first map, etc. The axes of each of the four maps are identical, one can clearly see that

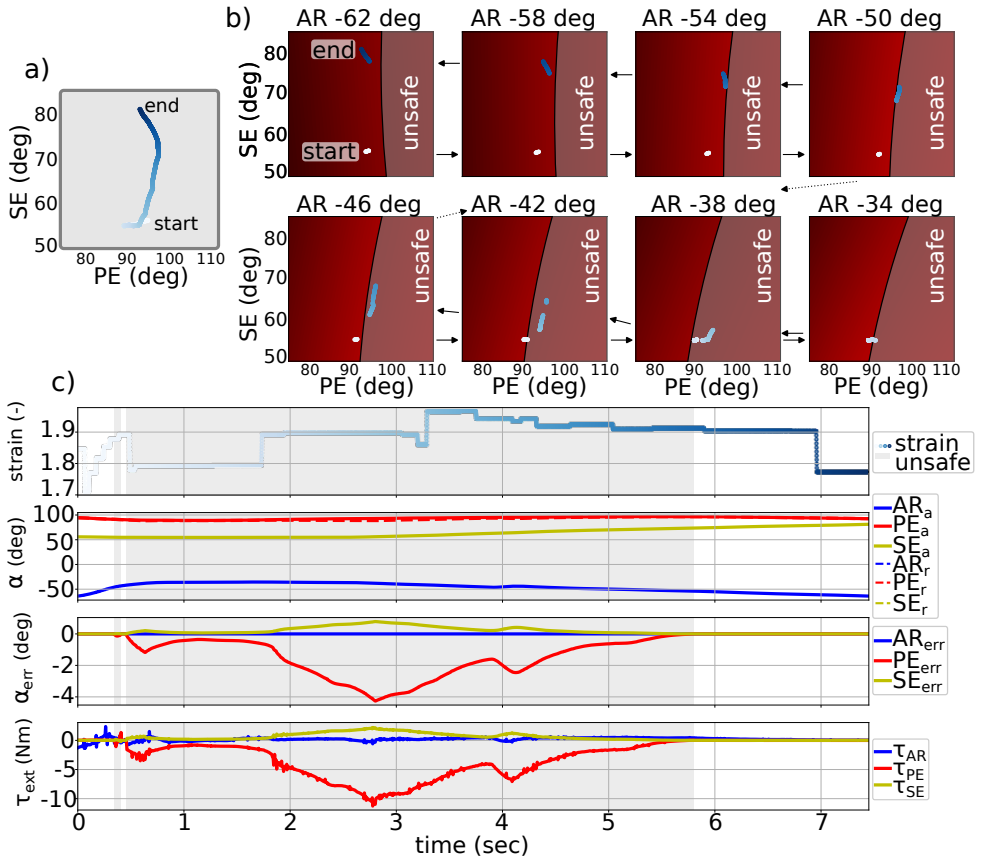

Fig. 10. Results of the experiment allowing free movement for all three shoulder state angles. The full trajectory in strain map coordinates is plotted in a). The zoomed in strain maps in b) show the trajectory and the unsafe zones, the color gradient of the trajectory matches with the first graph to indicate temporal coherence. The unsafe zones on the strain maps and time intervals when the subject was in an unsafe zone, are highlighted grey. The graphs in c) show the results of the experiment. The first graph shows the estimated strain during the experiment, where the color-gradient matches the trajectory on the strain maps, and the grey area indicates that the subject was in an unsafe zone at that time. The second graph shows the actual, α_a, and reference, α_r, shoulder state angles. The third graph shows the shoulder state angles errors used for the impedance controller. The bottom graph shows the resulting impedance control torques, acting on the subject, expressed in the directions of the shoulder state coordinates.

the unsafe zones are different from map to map, while the position on the maps stayed constant.

The first graph shows the experienced strain during the experiment, its color gradient matches the trajectory plot on the strain maps. The strain is nearly constant for each map interval, a) - d), as the position on the maps is unchanged. The position on the strain map, PE and SE, is shown on the four maps and can be seen to be constant during the experiment. This is also shown in the second graph which shows the actual and reference shoulder state angles over time. The third graph shows the shoulder state angles error, where AR_{err} is zero, and PE_{err} and SE_{err} change smoothly while changing strain maps and switching to the unsafe zone on these maps. The fourth graph shows the resulting shoulder state torques in all three shoulder DoF directions, they correspond to the shoulder state angle errors as is to be expected with impedance control.

The first of the three scenarios shown in this experiment is moving between safe points on adjacent strain maps, this occurred when the subject moved from the first strain map to the second, from a) to b). When the shoulder state angle on both maps is safe, the reference point is equal to α_a. There is no shoulder state error, which results in zero impedance control torques.

The second scenario, moving from a safe point to an unsafe point, starts halfway interval b), around 1.2 seconds, and lasts until approximately 2.2 seconds into the experiment. Here it switches from the first scenario, because the subject is now on the second strain map and moving towards the third strain map in which the subject would be inside an unsafe zone. The shoulder state angle errors slowly start increasing, as shown in the third graph, as the subject continues moving towards the unsafe map and the reference point is linearly interpolated between the safe and unsafe maps accordingly. The resulting shoulder state torques increase, alerting the subject that they are moving into an unsafe zone and guiding them to the nearest safe point.

Moving between unsafe points on adjacent strain maps is the third scenario shown in these results. This starts halfway interval c), at approx. 2.2 seconds, when the subject is in the unsafe zone on the third map and moving towards the unsafe zone in the fourth map. The reference point in the fourth map is farther away than the reference in the third map, the

linear interpolation between these points results in the slope of the shoulder state torques increasing, gradually increasing the guiding torques the subject experiences. This is executed in real-time, ensuring smooth transition between the reference points of both strain maps, thus the subject experienced smooth changes in the guiding torques.

The fourth scenario, moving to a safe point from an unsafe point, is not shown here, this is identical to moving from the third to the second map, and would result in the same graphs as shown mirrored around the y-axis.

D. Exp 3: Free movement

This experiment showcases our proposed method, combining the functionalities shown in the first two experiments, the subjects were free to move all three shoulder state angles, i.e., they were free to move on and between strain maps.

The results of this experiment are shown in Fig. 10. a) Shows the trajectory of the experiment, starting around 94.5 deg PE and 56 deg SE, and ending around 92.5 deg PE and 81 deg SE. The subject moved through eight strain maps, starting at -62 deg AR and rapidly moving to -34 deg AR, before moving back slowly to the starting strain map. These strain maps, and the path travelled on each map are shown in b). The trajectory is drawn as the white-to-blue gradient line and shown on each map when that was the closest map during the experiment, the unsafe zones are highlighted in grey. The graphs in c) show the strain, actual- and reference shoulder angles, shoulder angle error, and shoulder angle torques, respectively.

The subject moves into the unsafe zone on the map for AR -42deg right after the start of the experiment, the resulting joint state torques, τ_{ext}, guide the subject toward the closest safe point outside the zone. Around 2 seconds the subject moves to the map for AR -38deg and, as the zones changed with the map, is deeper into the zone, increasing the guiding torques. The subject then moved farther into the zone, resulting in the maximum shoulder state torques in PE and SE directions, just before three seconds of -11.3 Nm and 2.2 Nm, respectively. However, this did not result in the highest strain during the experiment, this is because the strain is based on the strain maps which assume no muscle activation. The actual strains would probably be higher in this case.

IV. Discussion

Our proposed method provides several key benefits. The most notable is allowing patient-led movement within the complete shoulder RoM, while the robot system guides the patient to safe poses when the rotator-cuff tendon strains are sufficiently high to increase the risk of re-injury. Additionally, the biomechanical model can easily be adjusted for patient-specific parameters, e.g., biometrics and injury recovery progress, resulting in high fidelity strain maps that are independent of task parameters. The patient can freely explore and expand their RoM and is no longer constrained to heuristic conservative limits or following a pre-planned trajectory.

The method is well suited for later stages of shoulder rehabilitation where the patient performs the exercises without supervision. Moreover, it is applicable even in early stages of rehabilitation, as the physiotherapist can move the patient through the exercises while the robot system manages biomechanical safety. The visual feedback can be used by physiotherapists to gain quantitative insight into the internal state of patients and to monitor recovery progress. It may be used by physiotherapists to safely expand the patients RoM, even in the early stages of rehabilitation.

While custom built robots/exoskeletons can have advantages over industrial collaborative robots in terms of RoM, higher payload, more DoF [5], [6], and possibly optimized mechanical design for specific task and kinematic constrains [7]. Mass-produced industrial collaborative robots still have significant advantages for use in assisted physical therapy. They are typically less costly and more readily available than task-specific robots, already meet strict safety criteria for human-robot interaction, and require little additional training to operate.

We have successfully shown that the proposed method is capable of guiding healthy subjects during assisted rotator-cuff rehabilitation using a biomechanically aware collaborative robot. However, before taking the next step of applying this work to actual clinical patients, there are some limitations that need to be addressed.

The strain maps used are based on the assumption that the subject passively moves around, and has no muscle activation. As the subject actively moves around, the actual strains will probably be higher than expected from the experiments. The strain maps are already precomputed for a large number of combinations and the full range (0 to 1) of muscle activation. However, solving for muscle activation based on external robot control, force, joint poses, and velocities is too computationally expensive to manage in real-time. Future work should be focused on updating the strain maps based on measured interaction force and joint parameters in real-time, for more accurate strain maps input to the biomechanical safety control.

Another limitation is the unknown accuracy of the rotator-cuff strains estimated through the biomechanical model. It has been compared to motion, forces, and muscle activity in healthy humans, it has not been applied, yet, to specifically estimating the strains of the rotator-cuff muscles. We are currently working on validating the model, including scaling to subject-specific metrics, this will be an important contribution going forward.

V. Conclusion

In this paper, we proposed a novel method for robot-assisted physical therapy for rehabilitation of rotator-cuff injury based on a high fidelity biomechanical model of the human. Real-time information on the human shoulder state angles was used to set the reference pose of the impedance controller based on the closest safe point on the strain maps, resulting in shoulder state torques guiding the subject away from high, unsafe, strain poses while the subject was free to move around. The proposed method has the potential to improve the safety, range of motion, and muscle activity that patients receive through robot-mediated physical therapy.

REFERENCES

[1] H. Minagawa, N. Yamamoto, H. Abe, M. Fukuda, N. Seki, K. Kikuchi, H. Kijima, and E. Itoi, "Prevalence of symptomatic and asymptomatic rotator cuff tears in the general population: from mass-screening in one village," *Journal of orthopaedics*, vol. 10, no. 1, pp. 8–12, 2013.

[2] T. Proietti, V. Crocher, A. Roby-Brami, and N. Jarrasse, "Upper-limb robotic exoskeletons for neurorehabilitation: a review on control strategies," *IEEE reviews in biomedical engineering*, vol. 9, pp. 4–14, 2016.

[3] L. Marchal-Crespo and D. J. Reinkensmeyer, "Review of control strategies for robotic movement training after neurologic injury," *Journal of neuroengineering and rehabilitation*, vol. 6, no. 1, p. 20, 2009.

[4] A. S. Niyetkaliyev, S. Hussain, M. H. Ghayesh, and G. Alici, "Review on design and control aspects of robotic shoulder rehabilitation orthoses," *IEEE Transactions on Human-Machine Systems*, vol. 47, no. 6, pp. 1134–1145, 2017.

[5] B. Kim and A. D. Deshpande, "An upper-body rehabilitation exoskeleton Harmony with an anatomical shoulder mechanism: Design, modeling, control, and performance evaluation," *The International Journal of Robotics Research*, vol. 36, no. 4, pp. 414–435, Apr. 2017.

[6] N. Jarrasse and G. Morel, "Connecting a Human Limb to an Exoskeleton," *IEEE Transactions on Robotics*, vol. 28, no. 3, pp. 697–709, Jun. 2012.

[7] A. Schiele and F. C. T. van der Helm, "Kinematic Design to Improve Ergonomics in Human Machine Interaction," *IEEE Transactions on Neural Systems and Rehabilitation Engineering*, vol. 14, no. 4, pp. 456–469, Dec. 2006.

[8] N. Hogan, "Impedance control - An approach to manipulation. I - Theory. II - Implementation. III - Applications," *ASME Transactions Journal of Dynamic Systems and Measurement Control B*, vol. 107, pp. 1–24, Mar. 1985.

[9] S. Hussain, P. K. Jamwal, M. H. Ghayesh, and S. Q. Xie, "Assist-as-needed control of an intrinsically compliant robotic gait training orthosis," *IEEE Transactions on Industrial Electronics*, vol. 64, no. 2, pp. 1675–1685, 2016.

[10] A. U. Pehlivan, D. P. Losey, and M. K. O'Malley, "Minimal assist-as-needed controller for upper limb robotic rehabilitation," *IEEE Transactions on Robotics*, vol. 32, no. 1, pp. 113–124, 2015.

[11] C. Wang, L. Peng, Z. G. Hou, W. Wang, and T. Su, "A Novel Assist-As-Needed Controller Based on Fuzzy-Logic Inference and Human Impedance Identification for Upper-Limb Rehabilitation," in *2019 IEEE Symposium Series on Computational Intelligence (SSCI)*, 2019, pp. 1133–1139.

[12] S. Haddadin, A. De Luca, and A. Albu-Schäffer, "Robot collisions: A survey on detection, isolation, and identification," *IEEE Transactions on Robotics*, vol. 33, no. 6, pp. 1292–1312, 2017.

[13] A. M. Zanchettin, P. Rocco, S. Chiappa, and R. Rossi, "Towards an optimal avoidance strategy for collaborative robots," *Robotics and Computer-Integrated Manufacturing*, vol. 59, pp. 47–55, 2019.

[14] H. Abidi and M. Cianchetti, "On Intrinsic Safety of Soft Robots," *Frontiers in Robotics and AI*, vol. 4, no. FEB, pp. 1–6, 2 2017. [Online]. Available: http://journal.frontiersin.org/article/10.3389/frobt.2017.00005/full

[15] C. Y. Chu and R. M. Patterson, "Soft robotic devices for hand rehabilitation and assistance: A narrative review," *Journal of NeuroEngineering and Rehabilitation*, vol. 15, no. 1, 2 2018. [Online]. Available: https://jneuroengrehab.biomedcentral.com/articles/10.1186/s12984-018-0350-6

[16] Y. Pan, H. Wang, X. Li, and H. Yu, "Adaptive Command-Filtered Backstepping Control of Robot Arms with Compliant Actuators," *IEEE Transactions on Control Systems Technology*, vol. 26, no. 3, pp. 1149–1156, 2018.

[17] S. Hong, C. Cho, H. Lee, S. Kang, and W. Lee, "Joint configuration for physically safe human–robot interaction of serial-chain manipulators," *Mechanism and Machine Theory*, vol. 107, pp. 246–260, 1 2017.

[18] S. Haddadin, S. Haddadin, A. Khoury, T. Rokahr, S. Parusel, R. Burgkart, A. Bicchi, and A. Albu-Schaffer, "A truly safely moving robot has to know what injury it may cause," *IEEE International Conference on Intelligent Robots and Systems*, pp. 5406–5413, 2012.

[19] N. Mansfeld, M. Hamad, M. Becker, A. G. Marin, and S. Haddadin, "Safety map: A unified representation for biomechanics impact data and robot instantaneous dynamic properties," *IEEE Robotics and Automation Letters*, vol. 3, no. 3, pp. 1880–1887, 2018.

[20] L. Roveda, S. Haghshenas, M. Caimmi, N. Pedrocchi, and L. M. Tosatti, "Assisting operators in heavy industrial tasks: On the design of an optimized cooperative impedance fuzzy-controller with embedded safety rules," *Frontiers in Robotics and AI*, vol. 6, p. 75, 8 2019. [Online]. Available: https://www.frontiersin.org/article/10.3389/frobt.2019.00075/full

[21] S. Haddadin, S. Haddadin, A. Khoury, T. Rokahr, S. Parusel, R. Burgkart, A. Bicchi, and A. Albu-Schäffer, "On making robots understand safety: Embedding injury knowledge into control," *International Journal of Robotics Research*, vol. 31, no. 13, pp. 1578–1602, 11 2012. [Online]. Available: http://journals.sagepub.com/doi/10.1177/0278364912462256

[22] B. Busch, G. Maeda, Y. Mollard, M. Demangeat, and M. Lopes, "Postural optimization for an ergonomic human-robot interaction," in *IEEE International Conference on Intelligent Robots and Systems*. Vancouver: Institute of Electrical and Electronics Engineers Inc., 9 2017, pp. 2778–2785.

[23] A. G. Marin, M. S. Shourijeh, P. E. Galibarov, M. Damsgaard, L. Fritzsch, and F. Stulp, "Optimizing Contextual Ergonomics Models in Human-Robot Interaction," *IEEE International Conference on Intelligent Robots and Systems*, vol. 1, pp. 8603–8608, 2018.

[24] L. McAtamney and E. N. Corlett, "RULA: A survey method for the investigation of work-related upper limb disorders," *Applied Ergonomics*, vol. 24, no. 2, pp. 91–99, 1993.

[25] L. McAtamney and S. Hignett, "Rapid Entire Body Assessment (REBA)," *Applied Ergonomics*, vol. 31, pp. 201–205, 2000.

[26] W. Kim, J. Lee, L. Peternel, N. Tsagarakis, and A. Ajoudani, "Anticipatory Robot Assistance for the Prevention of Human Static Joint Overloading in Human-Robot Collaboration," *IEEE Robotics and Automation Letters*, vol. 3, no. 1, pp. 68–75, 2018.

[27] L. Peternel, C. Fang, N. Tsagarakis, and A. Ajoudani, "A selective muscle fatigue management approach to ergonomic human-robot co-manipulation," *Robotics and Computer-Integrated Manufacturing*, vol. 58, no. June 2018, pp. 69–79, 2019. [Online]. Available: https://doi.org/10.1016/j.rcim.2019.01.013

[28] L. F. C. Figueredo, R. C. Aguiar, L. Chen, S. Chakrabarty, M. R. Dogar, and A. G. Cohn, "Human Comfortability: Integrating Ergonomics and Muscular-Informed Metrics for Manipulability Analysis during Human-Robot Collaboration," *IEEE Robotics and Automation Letters*, vol. 6, no. 2, pp. 351–358, 2020.

[29] T. Petrič, L. Peternel, J. Morimoto, and J. Babič, "Assistive arm-exoskeleton control based on human muscular manipulability," *Frontiers in Neurorobotics*, vol. 13, no. May, 2019.

[30] F. Scotto di Luzio, D. Simonetti, F. Cordella, S. Miccinilli, S. Sterzi, F. Draicchio, and L. Zollo, "Bio-cooperative approach for the human-in-the-loop control of an end-effector rehabilitation robot," *Frontiers in neurorobotics*, vol. 12, p. 67, 2018.

[31] D. Simonetti, L. Zollo, E. Papaleo, G. Carpino, and E. Guglielmelli, "Multimodal adaptive interfaces for 3d robot-mediated upper limb neuro-rehabilitation: An overview of bio-cooperative systems," *Robotics and Autonomous Systems*, vol. 85, pp. 62–72, 2016.

[32] J. M. Prendergast, S. Balvert, T. Driessen, A. Seth, and L. Peternel, "Biomechanics Aware Collaborative Robot System for Delivery of Safe Physical Therapy in Shoulder Rehabilitation," *IEEE Robotics and Automation Letters*, vol. 6, 2021.

[33] H. Østerås and T. A. Torstensen, "The dose-response effect of medical exercise therapy on impairment in patients with unilateral longstanding subacromial pain," *The Open Orthopaedics Journal*, vol. 4, p. 1, 2010.

[34] A. Seth, J. L. Hicks, T. K. Uchida, A. Habib, C. L. Dembia, J. J. Dunne, C. F. Ong, M. S. DeMers, A. Rajagopal, M. Millard *et al.*, "OpenSim: Simulating musculoskeletal dynamics and neuromuscular control to study human and animal movement," *PLoS computational biology*, vol. 14, no. 7, p. e1006223, 2018.

[35] A. Seth, M. Dong, R. Matias, and S. Delp, "Muscle Contributions to Upper-Extremity Movement and Work From a Musculoskeletal Model of the Human Shoulder," *Frontiers in Neurorobotics*, vol. 13, Nov. 2019.

[36] M. Ester, H. P. Kriegel, J. Sander, and X. Xu, "A Density-Based Algorithm for Discovering Clusters in Large Spatial Databases with Noise," in *Proceedings of the 2nd International Conference on Knowledge Discovery and Data Mining*. AAAI Press, 1996, p. 226–231.

[37] R. P. Brent, "Algorithms for minimization without derivatives, chap. 4," 1973.

[38] A. Albu-Schaffer, C. Ott, U. Frese, and G. Hirzinger, "Cartesian impedance control of redundant robots: Recent results with the DLR-light-weight-arms," in *2003 IEEE International Conference on Robotics and Automation*, vol. 3, 2003, pp. 3704–3709.

A

Appendix - Online Biomechanical Control

A.1. Unsafe zone check

For each timestep we need to check whether the point on the strain map is in an unsafe zone. The ellipses are precomputed as detailed in the paper using the Minimum Volume Enclosing Ellipse (MVEE) method, this returns the ellipses in terms of their parameters as used and described here. We use the ellipse inequality to check whether a point is inside the ellipse, thus unsafe, as

$$\left(\underline{p}-\underline{c}\right)^{T}\mathbf{A}\left(\underline{p}-\underline{c}\right)<1, \tag{A.1}$$

where **A** is the matrix of the ellipse equation in center form, $\underline{c}$ is the center of the ellipse, (x_0, y_0) in Fig. A.1, and $\underline{p}=[p_x,p_y]$ is the point on the map we want to check. If this is true, the point $\underline{p}$ is inside the ellipse.

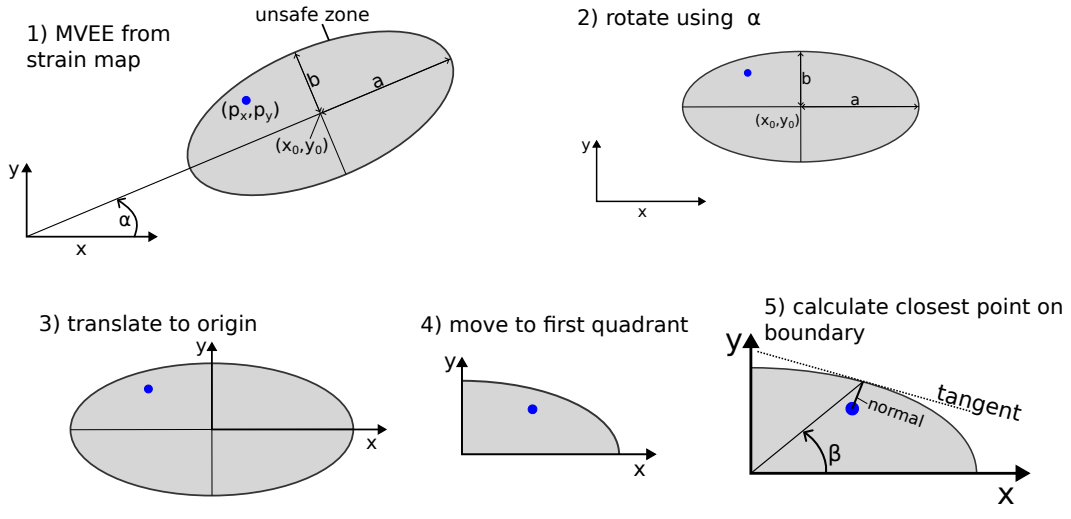

Figure A.1: How to calculate the closest point on ellipse contour. 1) shows the original ellipse from the precomputation using the MVEE method and the current point inside the ellipse. In 2) the ellipse is rotated such that the major semi-axis is aligned with the x-axis. In 3) the ellipse and point are translated such that the center of the ellipse is on the origin. The point is translated to the first quadrant of the ellipse in 4), this means there is only one solution for finding a line perpendicular to the ellipse contour that intersects the point. In 5) the closest point on the ellipse contour is calculated using the tangent to the contour and the line from the point to the contour.

A.2. Calculate reference point on ellipse contour

When the current strain map point is inside an ellipse, thus unsafe, we calculate the closest safe point, which is the closest point on the ellipse contour. We use the ellipse equation

$$\underline{x}(\beta) = [\mathrm{a}\cos\beta, \mathrm{b}\sin\beta]^T \tag{A.2}$$

where a is the semi-major axis, b is the semi-minor axis, and β is the angle, Fig. A.1 (5). We first have to make it a squared ellipse, where the major-semi axis is aligned with the x-axis, to use this equation. To do this, we first rotate the ellipse and point $\underline{\mathrm{p}}$ using the ellipse angle α. Then we translate it to the frame origin. We translate the point to the first quadrant of the ellipse, as this means there is only one solution when solving for tangent lines to the ellipse contour with their normal intersecting the point $\underline{\mathrm{p}}$ (instead of four solutions).

When the normal to the tangent of the ellipse contour (A.2) intersects point $\underline{\mathrm{p}}$. The tangent of the ellipse contour is the derivative of $\underline{\mathrm{x}}$, as

$$\underline{x}'(\beta) = [-\mathrm{a}\sin\beta, \mathrm{b}\cos\beta]^T. \tag{A.3}$$

This has to be perpendicular to the line from $\underline{\mathrm{p}}$ to $\underline{\mathrm{x}}$: $(\underline{p} - \underline{x}) \cdot \underline{x}' = 0$. Solving using Brent's method [1] on the interval $\beta \in [0, \pi/2]$ to estimate the zero of $f(\beta)$, as

$$f(\beta) = (a^2 - b^2)\sin\beta\cos\beta - \mathrm{a} * \mathrm{p}_x * \sin\beta + \mathrm{b} * \mathrm{p}_y * \sin\beta.$$

Solving this for β and substituting in (A.2), returns the coordinates of the closest safe point. We then reverse the operations, by moving this point to the original quadrant, translating it from the origin to the ellipse center and rotating back with α.

B

Appendix - Frame Transformations

B.1. Shoulder State Angles to End Effector Pose

To calculate the Robot end effector pose from the shoulder state angles, we construct the transformation matrix from the rotation matrix, $\mathbf{R}_{EE}$, which rotates from end effector frame to the robot base frame, and the origin, $\underline{o}_{EE}$, of the end effector frame. The frames and shoulder state angles are shown in Fig. B.1.

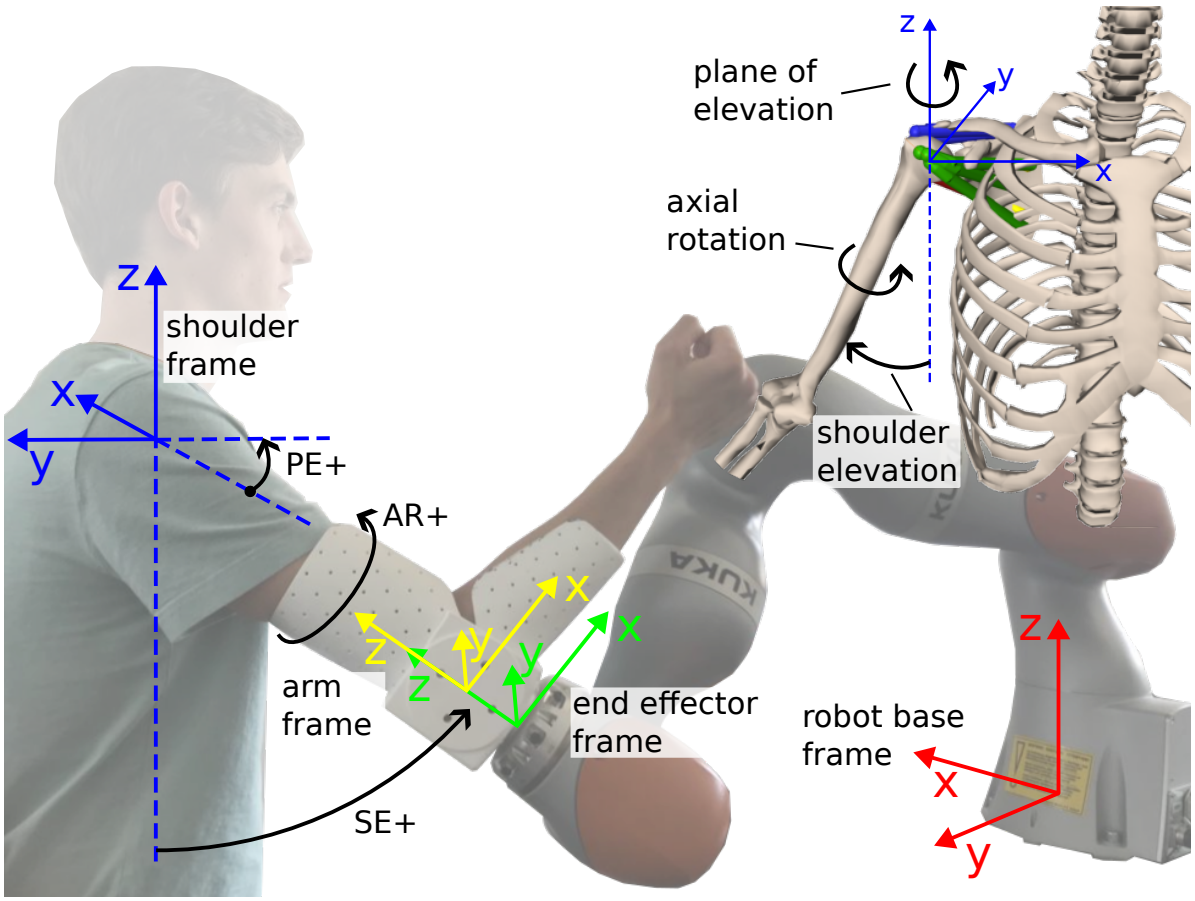

Figure B.1: Figure showing the shoulder state angles, and the various frames used to convert between shoulder state angles and end effector pose.

The orientation matrix follows from a series of rotations, shown in Fig. B.2. And can be calculated as

$$\mathbf{R}_{EE} = {}^{Base}\mathbf{R}_{shoulder}\mathbf{R}_z(-\pi/2)\mathbf{R}_z(PE)\mathbf{R}_x(-SE)\mathbf{R}_z(AR), \tag{B.1}$$

where ${}^{Base}\mathbf{R}_{shoulder}$ is the orientation matrix of the shoulder frame, which is constant in time and known. The other matrices are standard rotations around the indicated axis with the indicated angle, $\mathbf{R}_{axis}(angle)$.

The orientation of the arm frame and end effector frame are identical. However, the origins are not, these can be calculated as

$$\underline{o}_{EE} = \mathbf{R}_{EE} \cdot \underline{L}_{EE} + \underline{o}_{shoulder} \tag{B.2}$$

where $\underline{o}_{EE}$ is the origin of the End Effector in the robot base frame, $\underline{o}_{shoulder}$ is the origin of the shoulder frame in the base frame which is known and constant, and $\underline{L}_{EE}$ is the vector from the shoulder origin to the origin of the default arm frame (where all angles are zero), which is $[0, 0, -L_{arm}]^T$ for the origin of the arm frame and $[0, 0, -L_{Sh\_to\_EE}]^T$ for the end effector origin.

B.2. End Effector Pose to Shoulder State Angles

The shoulder state angles were calculated using the orientation matrix of the end effector frame. This was read in real-time and used to estimate the shoulder angles. By rewriting (B.1), we can use the known end effector and shoulder frames orientation matrices to solve for the three shoulder state angles.

$\mathbf{R} = \mathbf{R}^T_{shoulder}\mathbf{R}_{EE}$, where $r_{i,j}$ indicate the element on the i-th row and j-th column. And using $\mathbf{R}$ to solve for the shoulder state angles as

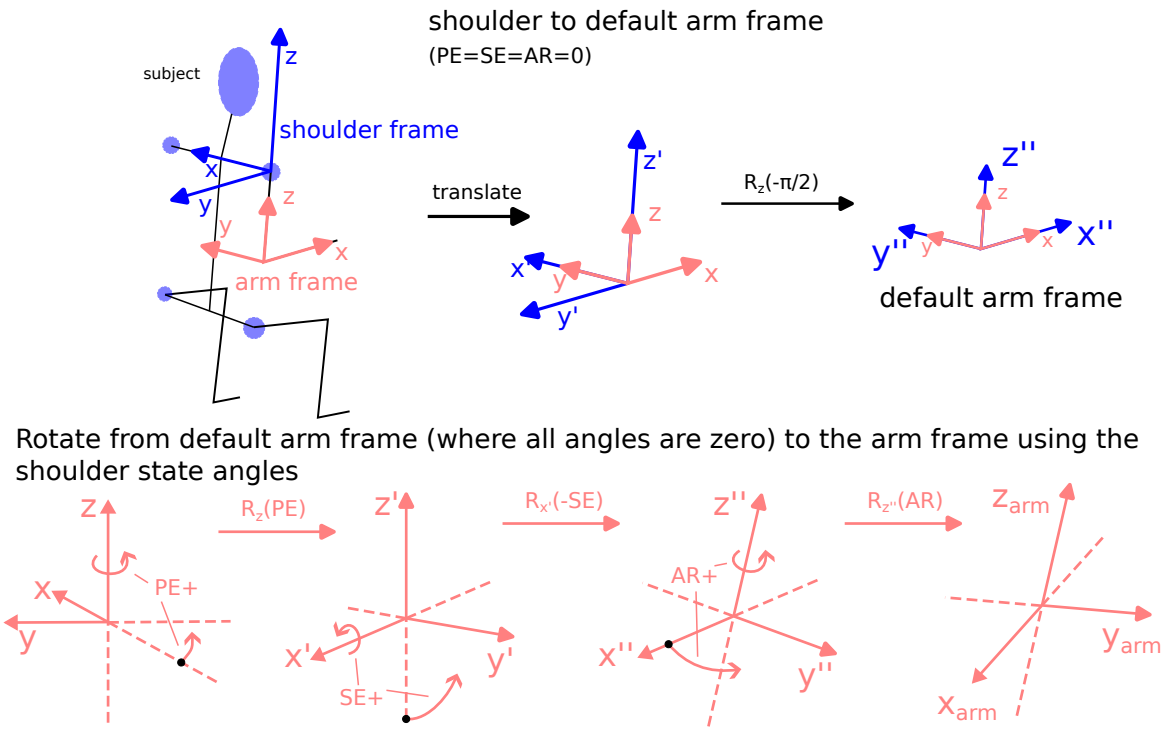

Figure B.2: Showing the shoulder and default arm frames, the conversion between them. And how the arm (thus end effector frame) can be calculated from the shoulder state angles.

$$\text{PE} = atan2\left(r_{2,3}, r_{1,3}\right),$$
$$\text{SE} = atan2\left(\sqrt{r_{1,3}^2 + r_{2,3}^2}, r_{3,3}\right),$$
$$\text{AR} = atan2\left(-r_{3,1}, -r_{3,2}\right).$$

B.3. Shoulder State Torques from End Effector Force

For data processing we transform the End Effector force to torques on the shoulder in the direction of the three shoulder state angles. The End Effector force is expressed as ${}^{base}\underline{F}_{EE}$ (N), and the End Effector moments as ${}^{base}\underline{M}_{EE}$, both expressed in the base frame.

We first compute the torques on the shoulder joint resulting from the moments on the End Effector as

$${}^{sphere}\underline{M}_{EE} = {}^{sphere}\mathbf{R}_{shoulder} * {}^{shoulder}\mathbf{R}_{base} * {}^{base}\underline{M}_{EE}$$

where ${}^{sphere}\mathbf{R}_{shoulder}$ transforms from the shoulder to the sphere frame and is calculated as $(\mathbf{R}_z(PE - \pi/2)\mathbf{R}_x(-SE)\mathbf{R}_z(-\pi/2))^T$.

The resulting moments on the shoulder from the end effector force vector are calculated as

$${}^{sphere}\underline{M}_{shoulder} = \left({}^{sphere}\mathbf{R}^T{}_{shoulder} * \underline{L}_{EE}\right) \times \left({}^{base}\mathbf{R}^T{}_{shoulder} * {}^{base}\underline{F}_{EE}\right)$$

where ${}^{sphere}\underline{M}_{shoulder}$ are the moments on the shoudler origin resulting from the end effector forces, expressed in the sphere frame in Nm.

The shoulder state torques are then defined as

$$\tau_{\text{PE}} = {}^{sphere}\underline{M}_{EE}[z],$$
$$\tau_{\text{SE}} = {}^{sphere}\underline{M}_{shoulder}[x],$$
$$\tau_{\text{AR}} = -{}^{sphere}\underline{M}_{shoulder}[y].$$

Bibliography

[1] R. P. Brent, “Algorithms for minimization without derivatives, chap. 4,” 1973.